Silicon photonic olfactory sensor based on an array of 64 biofunctionalized Mach-Zehnder interferometers

Loic Laplatine, Maryse Fournier, Nicolas Gaignebet, Yanxia Hou, Raphael Mathey, Cyril Herrier, Jie Liu, Delphine Descloux, Bertrand Gautheron, Thierry Livache

▶ **To cite this version:**

Loic Laplatine, Maryse Fournier, Nicolas Gaignebet, Yanxia Hou, Raphael Mathey, et al.. Silicon photonic olfactory sensor based on an array of 64 biofunctionalized Mach-Zehnder interferometers. Optics Express, 2022, 30 (19), pp.33955. 10.1364/OE.461858 . hal-03852338

HAL Id: hal-03852338
https://hal.science/hal-03852338

Submitted on 14 Nov 2022

HAL is a multi-disciplinary open access archive for the deposit and dissemination of scientific research documents, whether they are published or not. The documents may come from teaching and research institutions in France or abroad, or from public or private research centers.

L'archive ouverte pluridisciplinaire **HAL**, est destinée au dépôt et à la diffusion de documents scientifiques de niveau recherche, publiés ou non, émanant des établissements d'enseignement et de recherche français ou étrangers, des laboratoires publics ou privés.

A silicon photonic olfactory sensor based on an array of 64 biofunctionalized Mach-Zehnder interferometers

LOIC LAPLATINE,[1,*] MARYSE FOURNIER,[1] NICOLAS GAIGNEBET,[1] YANXIA HOU,[2] RAPHAEL MATHEY,[2] CYRIL HERRIER,[3] JIE LIU,[3] DELPHINE DESCLOUX,[3] BERTRAND GAUTHERON ,[3] AND THIERRY LIVACHE[3]

[1] *Univ. Grenoble Alpes, CEA-LETI, 38054 Grenoble cedex, France*
[2] *Univ. Grenoble Alpes, CEA, CNRS, IRIG-SYMMES, 38000 Grenoble, France*
[3] *Aryballe, 38000 Grenoble, France*
[*] *loic.laplatine@cea.fr*

Abstract: Silicon photonics can address a variety of applications, from datacom and biosensing to lidars. Recently, this technology has been explored for gas sensing. Detection and identification of odors remains a critical challenge in diverse areas such as air quality, food spoilage or personal well-being. In this work, we present an olfactory sensor based on an array of 64 biofunctionalized Mach-Zehnder interferometers integrated on a silicon nitride platform. The ability to analyze odors at ppm level is demonstrated for several volatile organic compounds.

© 2022 Optica Publishing Group under the terms of the Optica Publishing Group Publishing Agreement

1. Introduction

Silicon Photonics is now becoming a mature technology with diverse applications ranging from telecommunication [1, 2] and lidars [3] to biosensors [4, 5]. The ability to guide light into sub-micron silicon or silicon nitride waveguides allows the design of compact photonic integrated circuits that can be mass-produced at low cost by leveraging the CMOS industry.

Many simple gas molecules exhibit sharp absorption lines in the near to mid infrared which can be used to design specific sensors [6, 7]. However, multiplexing is limited by the number of laser sources with different wavelengths which can be implemented on a single system, typically a few tens [8]. Olfaction, on the other hand, implies the detection and identification of thousands of different odors which are made of volatile organic compounds (VOC). As in mammal olfaction, artificial noses rely on a limited number of non-specific sensors with different physicochemical properties [9]. The global response to a given VOC or VOC mixture, called a signature, correlates to a specific odor. In contrast with analytical approaches, artificial noses do not try to identify which molecules compose an odor, nor their relative concentrations. Instead, odor identification is made possible by searching for similar signatures in a database. For instance, by using nearly 400 different types of olfactory receptors, human olfaction can differentiate millions of different odors [10], some of them at sub ppb concentrations [11].

Traditional electronic noses (e-nose) rely on metal oxide semiconductors or polymers. We recently introduced a surface plasmon resonance imaging (SPRi)-based e-nose using organic molecules and short peptides as bioreceptors [12, 13]. Herein, we present a silicon photonic platform optimized for this application with Mach-Zehnder interferometers (MZI) biofunctionalized with these bioreceptors. With a bulk limit of detection (LoD) in the 10^{-7} RIU range, our sensor enables odor detection and identification at ppm level.

In silicon photonics, refractive index-based sensing has been demonstrated with several transducing components, typically microring resonators (MRR), interferometers, Bragg gratings and photonic crystals [14]. Among these, MZI have shown great promise in terms of LoD and

readout simplicity [15–19]. While most silicon photonic sensors target aqueous samples for the health and agri-food industries, less work has been devoted to VOC detection in gas phase.

First developments in the early 90s' were made on MZI based on ion-exchange glass waveguides coated by a 1-µm-thick polymer films to detect perchloroethylene with a LoD near 100 ppm [20]. More recently, a 240-nm-thick porous metal oxide (ZnO) layer was deposited on MRR to detect ethanol vapors [21]. MRR coated with polymer layers were also developed to detect acetone and toluene with LoD in the 10 ppm range [22], as well as CO_2 with LoD of 370 ppm [23]. Methane detection at a few ppm was shown using MZI with a polymer cladding doped with cryptophane-A [24]. LoD down to the ppb range was demonstrated by photonic crystals coated by a 60-nm-thick fluoroalcohol polysiloxanes polymer layer for the detection of nerve agent simulant methyl salicylate [25]. To enhance the sensitivity, the thickness of the functionalization layer should ideally extend slightly above the penetration depth of the electric field around the waveguide. By using porous SiO_2 layers, ethanol vapor measurement in the ppb range has been recently demonstrated [26]. Note that all these interferometric VOC sensors are based on the refractive index change of a sensing film. However, the thicker the film, the longer the VOC will take to diffuse down to the waveguide surface where the evanescent field is maximum. For films hundreds of nanometers thick, full response can take tens of seconds, which is a drawback for real-time assessment of intermittent odor sources, odor tracking or for low volume samples. Moreover, porous layers make localized biofunctionalization more difficult.

To the best of our knowledge, so far all silicon photonic VOC sensors were designed to target specific or unspecific detection of only a few VOC, without multiplexing nor ability to discriminate between different odors.

2. Mach-Zehnder interferometer working principle

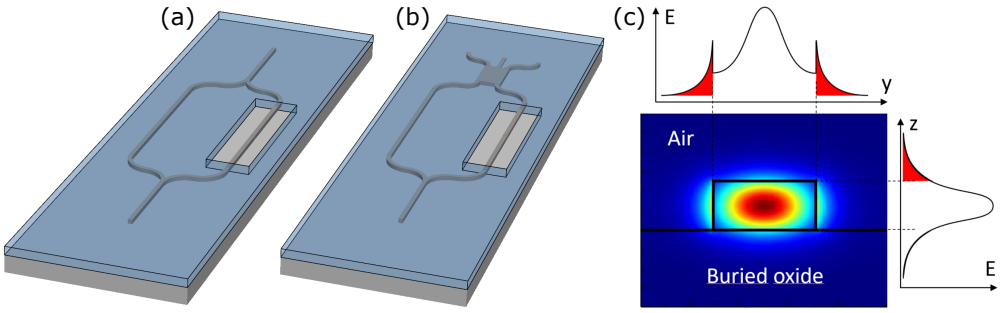

Fig. 1. (a) Standard MZI with one input and one output optical port. (b) Coherent MZI based on a 120° hybrid with three optical outputs. The oxide cladding opening window defines the sensing waveguide. (c) Simulation of the electric field intensity of a 250-nm-high 460-nm-wide Si_3N_4 waveguide in the fundamental TE mode. The evanescent tail of the electric field interacting with the environment is highlighted in red.

An integrated MZI is schematically represented in Figure 1. The light from a continuous-wave laser source at a fixed power and wavelength is split between the reference arm and the sensing arm with length L_r and L_s and effective index n_{eff-r} and n_{eff-s}, respectively. A typical MZI has the reference arm cladded in oxide while the sensing arm is exposed to the sensing medium through an oxide-opening window. In each arm, the light accumulates a phase delay ϕ_r and ϕ_s proportional to the arm length and effective index. The light also suffers from attenuation because of waveguide losses α_r and α_s. Recombining the light from the two arms results in interferences, leading to a sinusoidal transmission I varying with the phase delay difference Φ

between the two arms (Eq. 1-4). In practice, the initial phase has no importance, and only the phase shift $\Delta\Phi$ is recorded.

The parameter V in Eq. 1-2 is the visibility of the interferences, and varies from 0 to 1. In the best case, when V tends to 1, complete extinction occurs for destructive interferences. The intensity variations are thus maximized between constructive and destructive interferences, and $I = cos^2(\Phi/2)$. In the worst case, when V tends to 0, the intensity tends toward a fixed value and interferences become impossible to observe. Note that visibility only affects the noise of the phase shift monitoring, not the phase sensitivity itself. Visibility can be maximized by using low-loss or short waveguides, by setting the arm length ratio to $L_r/L_s = \alpha_s/\alpha_r$, or by compensating the loss difference using a custom splitting ratio. In silicon photonics, it is common to refer to the MZI extinction ratio $ER = I_{max}/I_{min} = 1+V/1-V$.

$$I \propto \frac{1}{2}[1 + V \cdot cos(\Phi)] \tag{1}$$

$$V = \frac{2 \cdot e^{-\frac{1}{2}(\alpha_s L_s + \alpha_r L_r)}}{e^{-\alpha_s L_s} + e^{-\alpha_r L_r}} \tag{2}$$

$$\Phi = \phi_s - \phi_r = \frac{2\pi}{\lambda}(L_s \cdot n_{eff-s} - L_r \cdot n_{eff-r}) \tag{3}$$

$$\Delta\Phi = \Phi(t) - \Phi(t = 0) = \frac{2\pi}{\lambda} \cdot L_s \cdot \Delta n_{eff-s}(t) \tag{4}$$

The phase sensitivity of a MZI (in rad/nm) to a thin adlayer of thickness h can then be expressed as in Eq. 5a:

$$\frac{\partial\Delta\Phi}{\partial h} = \frac{2\pi}{\lambda} \cdot L_s \cdot \frac{\partial n_{eff-s}}{\partial h} = \frac{2\pi}{\lambda} \cdot L_s \cdot S_{surface} \tag{5a}$$

with the surface sensitivity $S_{surface}$ in RIU/nm. Eq. 5a indicates that the phase sensitivity of the MZI is both proportional to the length of the sensing arm and to the surface sensitivity of the sensing waveguide. The latter depends on the overlap of the evanescent tail of the optical mode with the environment in the vicinity of the waveguide.

It is also convenient to introduce the phase sensitivity of a MZI to a bulk refractive index change of the cladding medium, as expressed as in Eq. 5b:

$$\frac{\partial\Delta\Phi}{\partial n_{clad}} = \frac{2\pi}{\lambda} \cdot L_s \cdot \frac{\partial n_{eff-s}}{\partial n_{clad}} = \frac{2\pi}{\lambda} \cdot L_s \cdot S_{bulk} \tag{5b}$$

with the bulk sensitivity S_{bulk} expressed in RIU/RIU. S_{bulk} corresponds to the change of waveguide effective index with respect to a change of cladding refractive index. Because the refractive indices of the materials and the effective indices of the waveguides vary with the wavelength, it can be shown from Eq. 1 and 3 that the MZI transmission also varies with λ. Eq. 6 indicates the spectral distance between two successive interferences, called the Free Spectral Range (FSR):

$$FSR(\lambda) = \frac{\lambda^2}{L_r \cdot n_{g-r}(\lambda) - L_s \cdot n_{g-s}(\lambda)} \tag{6}$$

Where $n_g(\lambda) = n_{eff}(\lambda) - \lambda\frac{\partial n_{eff}(\lambda)}{\partial\lambda}$ is the group index of the waveguide. For MZI operated at a fixed wavelength, it is worth having a large FSR compared to the spectral line-width and wavelength jitter or drift of the laser (the typical spectral drift of semiconductor lasers is 60-100 pm/K) [19]. The FSR can be made infinite at a given wavelength by setting the arm

length ratio to $L_s/L_r = n_{g-r}/n_{g-s}$. For wavelength-modulated MZI, the FSR has to be smaller than the wavelength scanning window [27].

Variation of the die temperature also affects the signal $\Delta\Phi$ [28]:

$$\frac{\partial \Delta\Phi}{\partial T} = \frac{2\pi}{\lambda}\left(L_s \cdot \frac{\partial n_{eff-s}(T)}{\partial T} - L_r \cdot \frac{\partial n_{eff-r}(T)}{\partial T}\right) \tag{7}$$

Eq. 7 shows that athermal behavior can be achieved (in a first approximation) by choosing the ratio of arm length so that:

$$\frac{L_s}{L_r} = \frac{\frac{\partial n_{eff-r}(T)}{\partial T}}{\frac{\partial n_{eff-s}(T)}{\partial T}} \tag{8}$$

Therefore, a properly-designed MZI can significantly minimize both thermal and spectral sources of noise and drift while maintaining a high extinction ratio.

Eq. 1 also shows two drawbacks of a standard MZI. First, the sensitivity of the MZI output intensity with respect to phase variation, $\partial I/\partial\Phi$, varies as a sine function. Therefore, when Φ reaches integer values of π, the MZI sensitivity vanishes. Moreover, without wavelength or phase modulation [29], nor using a spectrometer [30], the direction of variation of Φ, whether it decreases or increases, is ambiguous due to the sine shape of the intensity. Fortunately, both issues can be solved by using a coherent detection scheme [15–19]. Compared to previously mentioned strategies which require either complex readout schemes or large on-chip spectrometers, 120° hybrid coherent detection only requires two additional optical outputs per MZI (Figure 1(b)). Acquisition frequency is mainly limited by the photodetector speed, and the multiplexing of tens of MZI remains possible on a small die. It is worth mentioning that the diffusion of VOC in air is orders of magnitude faster than for biomolecules in aqueous solutions. Therefore, the readout electronics must typically be able to monitor the phase shift at tens of Hz.

3. Photonic platform choice and PIC design

The most mature silicon photonics platforms address datacom applications where the wavelength ranges from 1.2 to 1.7 μm in order to minimize losses and dispersion in optical fibers. Silicon is thus the material of choice because of its transparency. However, for biological and gas sensing applications, silicon nitride ($n_{Si_3N_4} \approx 2$) exhibits a better trade-off than silicon ($n_{Si} \approx 3.5$) [31]. First, its lower intrinsic thermo-optical coefficient (TOC) reduces thermal noise and drift. Secondly, the lower index contrast with silicon dioxide ($n_{SiO_2} \approx 1.45$) reduces propagation losses. Finally, its transparency extends to the visible range, where absorption from water and gas is negligible. Wavelengths near 850 nm are a good compromise with low waveguide scattering loss and commercially available lasers and CMOS imagers, thus attracting a lot of interest from the biosensing community [32–35].

In order to design our devices, we studied the effect of the height and width of the sensing waveguide on its effective index and surface sensitivity at $\lambda \approx 850$ nm. Si_3N_4 waveguides with thicknesses ranging from 200 to 300 nm and widths from 300 to 800 nm were simulated using MODE solutions (ANSYS Lumerical, Inc.). Both the fundamental transverse electric (TE), i.e. with the electric field parallel to the die surface, and transverse magnetic (TM) modes were analyzed. An example of the electric field distribution in TE mode is shown in Figure 1(c). In order to limit the simulation time, the surface sensitivity $S_{surface}$ was extrapolated from the bulk sensitivity S_{bulk}, the penetration depth L_z and the refractive index of the adsorbed layer of VOC (Eq. 9-10), which was set at $n_{Ad} = 1.41$.

$$S_{surface} \approx (n_{Ad} - n_{clad})\frac{S_{bulk}}{L_z} \tag{9}$$

$$L_z = \frac{\lambda}{\sqrt{n_{eff}^2 - n_{clad}^2}} \tag{10}$$

S_{bulk} was calculated by comparing the effective index of the waveguide with a cladding index of 1 versus 1.05. As shown in Figure 2, the simulation shows that for both polarizations, thick and narrow waveguides exhibit the best surface sensitivity. However, such high aspect ratio waveguides suffer from higher propagation loss and are more difficult to fabricate with good reproducibility than lower aspect ratio waveguides. While the TE mode exhibits a higher sensitivity for waveguide aspect ratio above 1:2, the TM mode offers a more stable sensitivity under fabrication variability. Besides propagation loss and ease of fabrication, many other constraints should be taken into account to choose the right polarization for a given application.

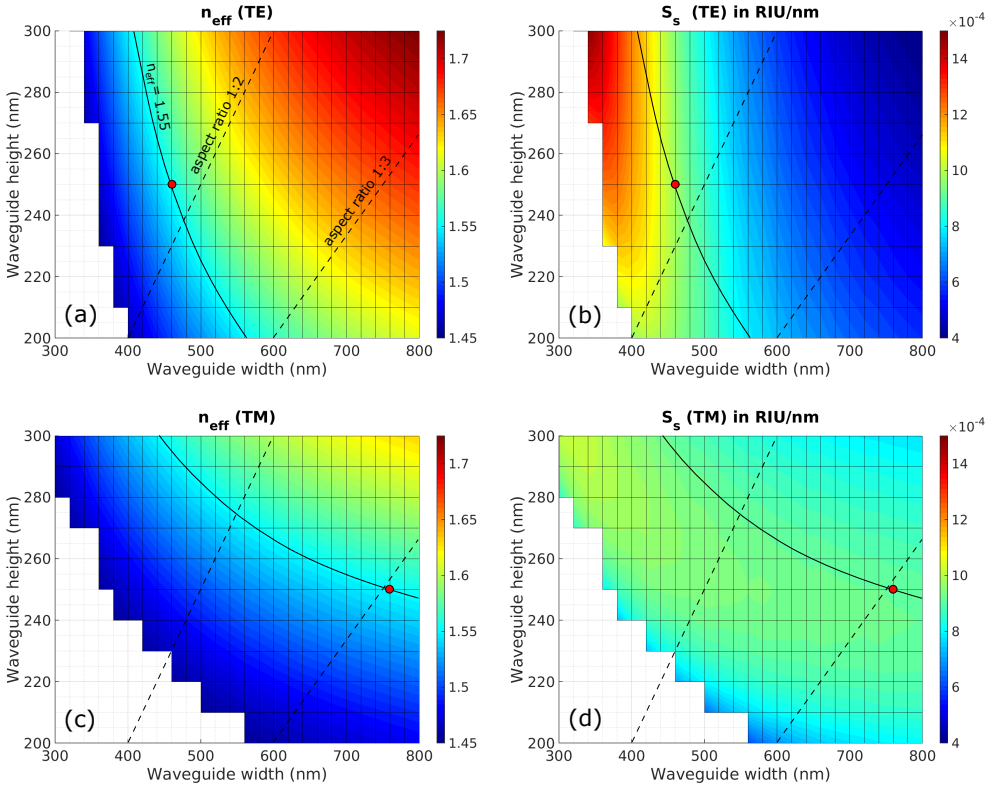

Fig. 2. Effective index (a and c) and surface sensitivity (b and d) simulations for Si_3N_4 waveguides (non-propagating modes with $n_{eff} \leq n_{SiO_2}$ are not shown) in TE and TM modes at Λ = 850 nm. Adlayer refractive index is set at n_{Ad} = 1.41. The straight dashed lines indicate the aspect ratio of the waveguide. The curved solid lines indicate sensing waveguide geometries for which n_{eff} = 1.55.

First, waveguides with low n_{eff} require a thicker BOX layer to avoid substrate leakage loss [36] when n_{eff} approaches n_{SiO_2}, thus increasing fabrication cost and grating coupler (GC) performance variability. Such waveguides also suffer from higher bend loss and crosstalk, which limit the design compactness, thus affecting die size and cost. Here, in TE mode, setting $n_{eff} \geqslant 1.55$ and keeping an aspect ratio near 1:2 leads to a waveguide height of 250 nm and a waveguide width of 460 nm with a surface sensitivity of 9.7×10^{-4} RIU/nm. In TM mode, since the surface sensitivity remains almost constant for n_{eff} = 1.55, we may choose the same

waveguide height as in TE mode, which leads to a waveguide width of 760 nm with a surface sensitivity of 9.1×10^{-4} RIU/nm. Although both configurations exhibit the same effective index and nearly the same surface sensitivity, the TM mode configuration suffers from higher bend loss (Figure 3(a)).

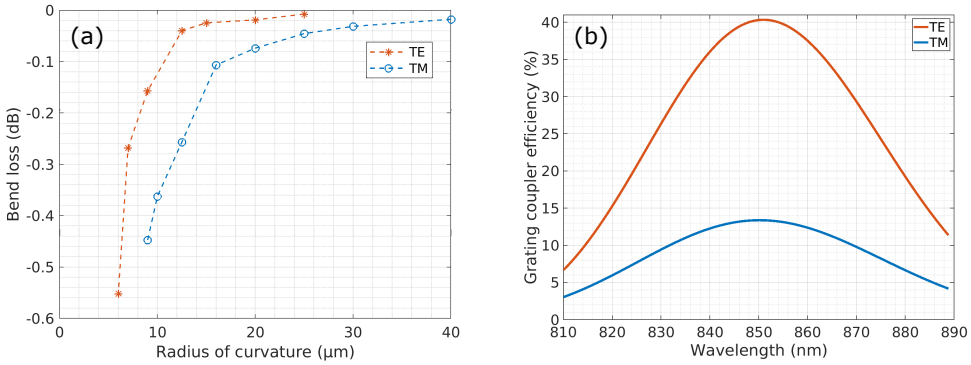

Fig. 3. (a) Simulated bend loss caused by mode mismatch for 250-nm-high sensing waveguides in TE and TM modes at λ = 850 nm. Waveguide widths are 460 nm and 760 nm in TE and TM modes, respectively. (b) Simulation of the GC efficiency for a single mode fiber with a mode field diameter of 5.3 µm in TE and TM mode. Optimized TE mode GC requires a 135-nm-deep partial etch of the Si_3N_4 layer and leads to simulated insertion loss of -3.9 dB. Optimized TM mode GC can be obtained with a full etch of the Si_3N_4 layer but shows an insertion loss limited to -8.7 dB.

Secondly, efficient coupling from a single mode fiber or a VCSEL to the photonic circuit is a critical point both for wafer-level characterization and for die-level packaging. GC were simulated and optimized with Rsoft FDTD (Synopsys, Inc.) for both polarizations. The 2D simulations were restricted to 250-nm-high cladded GC to be coupled to a single mode fiber with a mode field diameter of 5.3 µm at a standard incident angle of 8° inside the oxide cladding. The target wavelength was set to λ = 850 nm. In TE mode, using a 135-nm-deep partial etch of the Si_3N_4 layer, GC with a period of 577 nm and a filling factor of 50% can reach insertion loss as low as -3.9 dB (Figure 3(b)). In TM mode, the best insertion loss is limited to -8.7 dB and is reached for fully etched GC with a period of 630 nm and a filling factor of 58%.

With our Si_3N_4 platform, for gas sensing applications, a sensing waveguide with a height of 250 nm and a width of 460 nm in TE polarization emerges as a good compromise between ease of fabrication, bend loss, surface sensitivity and efficient coupling from a fiber or a VCSEL. The sensing waveguide length is set to 4.1 mm. The length of the reference waveguide is then adjusted to minimize the thermal sensitivity of the MZI and to reach FSR near 10 nm. Both arms are folded into spirals to minimize the MZI footprint. The width of the routing waveguides connecting each MZI to the optical input and outputs is set to 650 nm, close to the single mode cut-off, in order to decrease their propagation loss. GC are used to couple the light in and out of the dies. A series of 1×2 MultiMode Interference couplers (MMI) is used to equally distribute the input light into 64 identical MZI. Then, the same MMI are used to split the light between the reference and sensing waveguides of each MZI. Finally, 2×3 MMI are used to recombine the two arms into three output waveguides in which sine intensity variations are phase-shifted by $2\pi/3$.

4. Photonic circuits fabrication and biofunctionalization

The photonic circuits were fabricated on CEA-Leti's 200 mm CMOS platform. First, a 1.7-µm-thick thermal oxide was grown on silicon wafers. Then a 250-nm-thick layer of stoichiometric

silicon nitride was deposited by low-pressure chemical vapor deposition. Photonic circuit patterning in the Si_3N_4 layer was performed using 248 nm lithography and reactive ion etching (RIE). A first layer of oxide cladding was then deposited by SACVD followed by a CMP step. A second layer of oxide cladding was deposited by PECVD to reach a complete oxide thickness of 1.5 µm. A 200-nm-thick layer of PECVD SiN was finally deposited to protect the oxide cladding from humidity. Cladding opening windows were patterned using 248 nm lithography. RIE was used to etch the PECVD SiN and oxide down to the SACVD oxide. Wet etching was used to etch the remaining SACVD oxide to avoid damaging the sensing waveguides. Finally, a conformal 10-nm-thick layer of SiO_2 was deposited on the whole wafer by ion beam deposition for compatibility with the biofunctionalization process.

Peptides grafting was performed on the MZI array following the procedure described in the reference 37. First, the dies were activated by fresh piranha solution for 30 min and washed thoroughly with MilliQ water, followed by drying under Ar flow. Then, the silanization was performed in methanol with 2% (v/v) of 3-Aminopropyldimethylethoxysilane (APMDES, Gelest, cas: 18306-79-1) and 0.1% (v/v) of H_2O. After incubation for 1 hour, the dies were rinsed three times with methanol and isopropanol and then dried under Ar flow. Finally, the dies were annealed under 110°C for one hour.

Maleimide groups were then introduced on the silanized surface by incubating the dies in 1 mM solution of N-γ-maleimidobutyryl-oxysulfosuccinimide ester (sulfo-GMBS) in 50 mM phosphate buffer solution (PBS) at pH 8. After one hour of incubation at room temperature, the dies were rinsed with MilliQ water and dried under Ar flow. Peptide grafting was performed locally by spotting the peptide solutions on the sensing arms using a Scienion sciFLEXARRAYER S12 robot. A typical spotting solution contains 1 mM of peptide in PBS (50 mM, pH 7). Dimethyl sulfoxide (DMSO) was added to help the solubilization in aqueous solution of certain peptides. After incubating overnight in a humidity chamber at room temperature, the dies were thoroughly rinsed with DMSO, H_2O and dried under Ar flow.

Photonic characterizations were performed at the wafer-level using a prober station (Elite300, FormFactor, Inc.) equipped with motorized single mode fiber holders. Spectra were acquired using a tunable laser source (Sacher Lasertechnik, Lion TEC-500-0850-030-M) and a powermeter (Newport, 1936-R, with a 918D-SL silicon cell) automated by a homemade LabVIEW program (National Instrument). At least 9 dies were tested per wafer. Measurement data were analyzed using Matlab (MathWorks, Inc.) and Python. Die level measurements were carried on a custom optical bench or with a NeOse Advance e-nose (Aryballe). The custom optical bench uses a VCSEL emitting at λ=850 nm aligned to the input GC, and a CMOS imager aligned to the 192 output GC. Olfactory signatures were extracted and analyzed using Aryballe Suite software. All concentrations of volatile compounds are given in molar ppm.

5. Results and discussion

Figure 4(a) shows a 22-mm-long and 4.7-mm-wide die. The photonic integrated circuit comprises a single input GC, an array of 64 MZI and an array of 192 output GC. Test structures for wafer-level prober characterization are also visible on the top and bottom parts of the die. Figure 4(b) shows a control quality image during the peptides spotting. As can be seen on a focused ion beam characterization in Figure 5(a), an overetch in the BOX layer was achieved by slightly extending the wet etch. That way, the sides of the waveguides are entirely exposed to the environment without interfering with the BOX surface. The waveguide sidewall angle is measured at 4°.

Figure 5(b) shows a scanning electron microscope image of a 4.1 mm-long sensing spiral waveguide. Note that the reference waveguide is located just 10 µm to the left but cannot be seen as it lies under the oxide cladding.

As shown in Figure 6(a), the propagation loss of routing oxide cladded waveguides is 1.0 dB/cm. The oxide cladding etching typically adds 0.5 dB/cm of propagation loss compared to bare

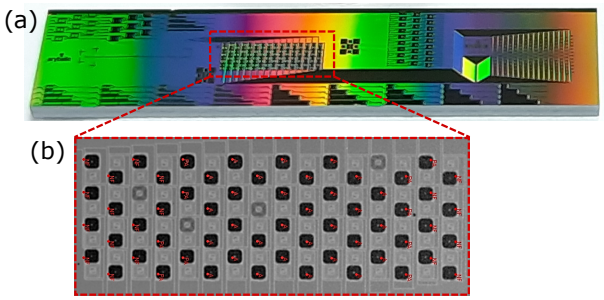

Fig. 4. (a) Picture of a die (22 mm × 4.7 mm). The optical input GC is located on the left, the 64 MZI array in the middle and the 192 output GC on the right. Test structures are also visible. (b) Droplets (in black, with red dot and labelling) of biofunctionalization solutions individually spotted on the sensing arms of the MZI array.

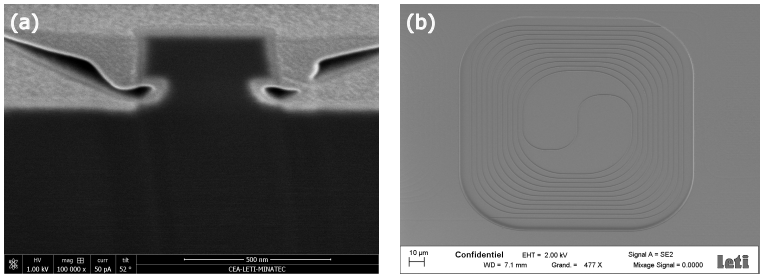

Fig. 5. (a) FIB cross section and (b) SEM image of a sensing waveguide.

waveguide before oxide cladding deposition. The final thin SiO_2 layer also adds between 0.2 and 1 dB/cm depending on the waveguide width. In both cases, the degradation of propagation loss is attributed to the increase of waveguide roughness. For MZI with arm lengths of only 4.1 mm, the extinction ratio ER reaches 18 dB at λ=850 nm (V ≈ 97%) and remains greater than 13 dB from 840 to 860 nm (Figure 6(b)).

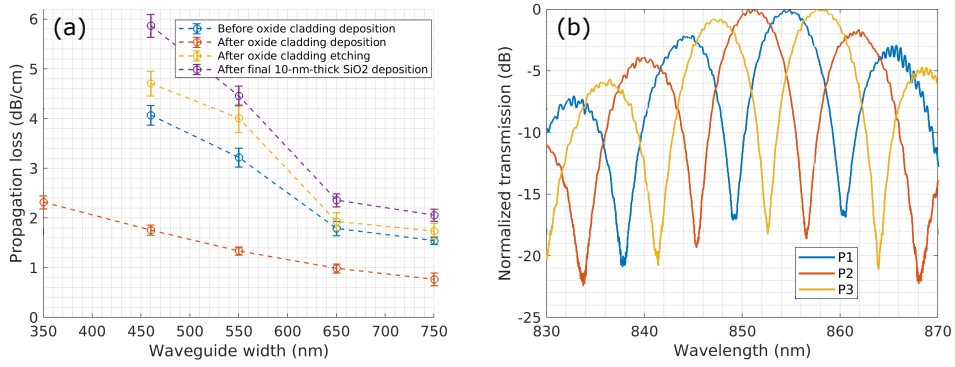

Fig. 6. (a) Propagation loss at λ = 850 nm. (b) Spectra of the three optical outputs of a coherent MZI.

A PTFE fluidic chamber is used to localize the gas flow onto the MZI array. Figure 7(a) shows the intensity variation of the three optical outputs of a single coherent MZI under the injection of

nonane vapors in ambient air on a non-functionalized die. After a blind phase calibration, the sensorgram corresponding to the phase shift $\Delta\Phi$ as a function of time is extracted unambiguously with a constant sensitivity regardless of the value of $\Delta\Phi$ thanks to the coherent phase scheme (Figure 7(b)). The sensorgram is recorded at 30 Hz and exhibits an electronic 3σ noise level of 3.5 mrad over 14 s.

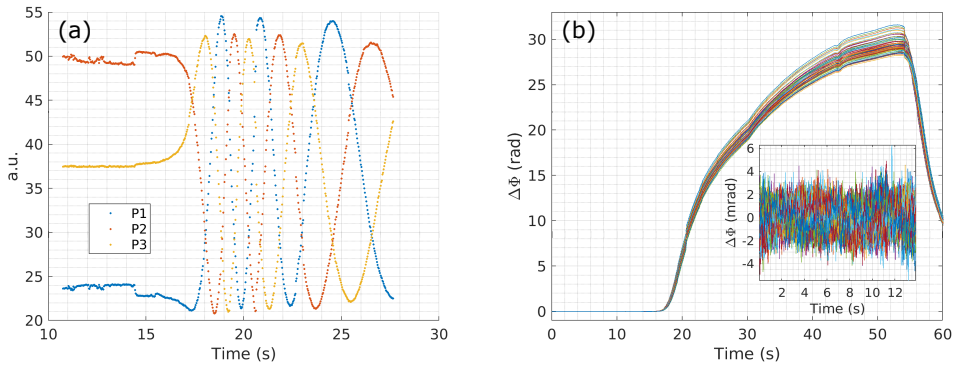

Fig. 7. (a) Optical outputs of a single coherent MZI measured when "sniffing" vapors of nonane at saturation in ambient air. (b) Corresponding sensorgram of 64 coherent MZI. The inset shows the baseline corrected by a 2nd order polynomial fit to remove the drift, showing a best-case 3σ noise level of 3.5 mrad (without frame averaging). Without polynomial fit, the 3σ noise level is 7.3 mrad.

As shown in Figure 8, the MZI exhibit a thermal sensitivity S_T ranging from -0.12 to -0.18 rad/°C in dry air when heated up from 26 to 57°C. We attribute this non-athermal behavior to the difference between the Si_3N_4 thermo-optical coefficient used in our simulations and its actual value.

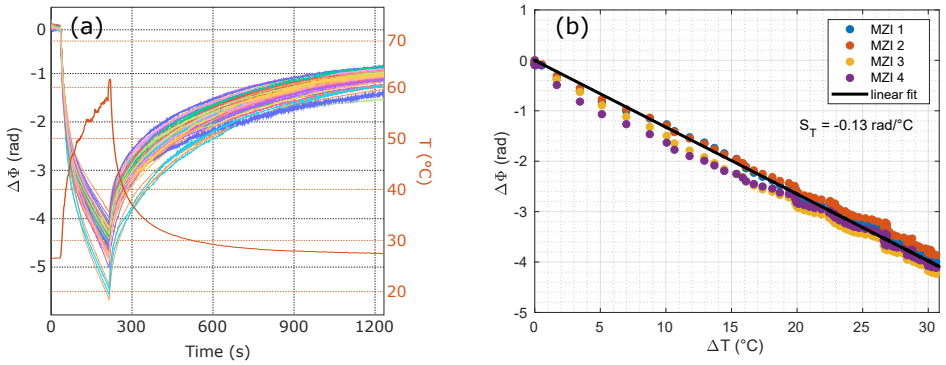

Fig. 8. (a) Sensorgram of the 64 MZI under a temperature variation of 30°C. (b) Thermal sensitivity S_T of the 4 non-functionalized MZI (as visible on Figure 4) calculated during the heating phase.

Since the refractive index of the air is a function of pressure (~3×10^{-4} RIU/bar), bulk sensitivity can be measured by pressure variations, without involving any VOC [38]. The MZI exhibit a bulk sensitivity S_{bulk} of 5530 ± 155 rad/RIU. This corresponds to an experimental LoD of 7×10^{-7} RIU. Dispersion of sensitivity between the different interferometers within an array is about 3%. It is worth noting that this sensitivity is not significantly modified by the grafting of

bioreceptors.

The bioreceptor-VOC interaction monitoring follows three different steps: first, a baseline with the refractive index of ambient air; then, the adsorption of the VOC until the equilibrium state is reached; and finally, desorption with the recovery of the initial surface refractive index. This leads to the typical sensorgram presented on Figure 9(a).

For an e-nose, the reversibility of the interaction is a key parameter in order to perform multiple independent measurements in series. As for SPRi, the reaction of the MZI sensors is remarkably fast. With image acquisition up to 60 Hz, events shorter than 100 ms can be detected, allowing for a fast recognition process [39]. The odor of a compound is characterized by its signature that can only be obtained with the multiplexed aspect of the sensor. This signature is shown in Figure 9(b) as a radar chart, resulting from the measurements of the biofunctionalized sensors exposed to a specific odorant sample. In such a signature, the radius of each point corresponds the mean signal intensity near equilibrium, i.e. the phase variation $\Delta\Phi$ of each MZI, as described in Eq. 11:

$$\Delta\Phi^i = S^i_{bulk} \times a^i_{VOC} \times \Delta X_{VOC} \tag{11}$$

where S^i_{bulk} is the bulk sensitivity of MZI i (rad/RIU); a^i_{VOC} is the affinity of MZI i to the VOC (RIU/ppm) and ΔX_{VOC} is the concentration variation of the VOC (ppm). The phase variation $\Delta\Phi^i$ of each MZI is then normalized to the minimum and maximum signal in the normalized signature (Figure 9(c)) using Eq. 12:

$$\Delta\Phi^i_{norm} = \frac{a^i_{VOC} - a_{min}}{a_{max} - a_{min}} \tag{12}$$

where $a_{min,max}$ are the minimum and maximum measured affinity among all MZI to the VOC. The evolution of the sensor response with respect to the concentration of VOC in Figure 10 was obtained using a dilution system based on Pulse Width Modulation (PWM) monitoring of valves [40]. The sensor sensitivity strongly depends on the VOC. For example, agrunitrile is detected with a sensitivity of 1.6 rad/ppm while Eucalyptol is detected with a sensitivity of 10^{-2} rad/ppm. This means that the system should be able to detect agrunitrile at ppb level while Eucalyptol would probably not be detected bellow 100 ppb.

This result, which seems counter-intuitive, reflects the surface aspect of the sensitivity of the sensor. In contrast, gas sensors based on absorbance exhibit responses directly proportional to

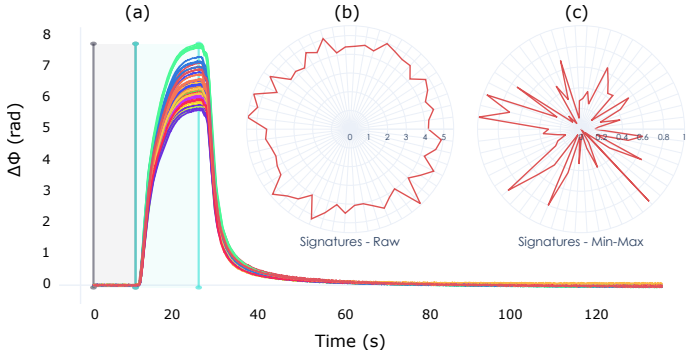

Fig. 9. (a) Sensorgram presenting the response of 64 sensors during the injection of a VOC in a carrier gas (ambient air). (b) Signature of the VOC is extracted from the response of each MZI during the presence of the VOC (inside the blue range). (c) Normalized signature independent of the VOC concentration.

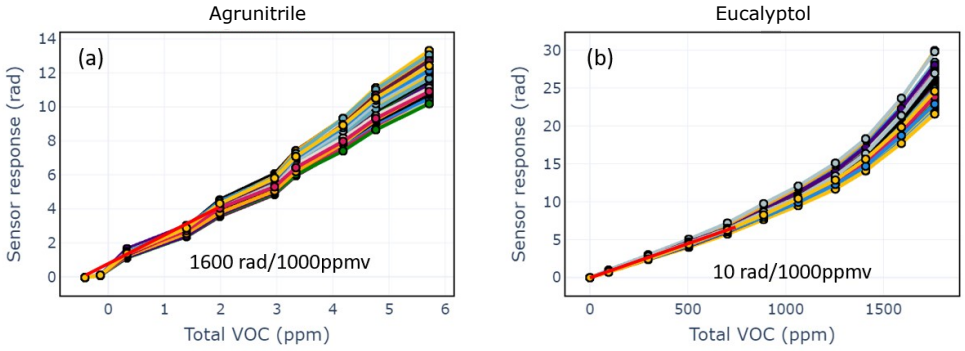

Fig. 10. Response of the sensor with increasing concentrations of Agrunitrile (a) and Eucalyptol (b). Each curve corresponds to a biofunctionalized MZI. VOC sensitivity is extracted from the slope of the average signal with respect to the concentration (red line).

the volume concentration of the VOC (Beer-Lambert law). Here, it is the variation of surface concentration which is measured. This surface concentration is assumed to be in equilibrium with the volume concentration. It follows a Langmuir model which depends on the physico-chemical properties of the VOC (in particular its vapor pressure) and on the chemical affinity (a^i_{VOC}) between the surface and the VOC.

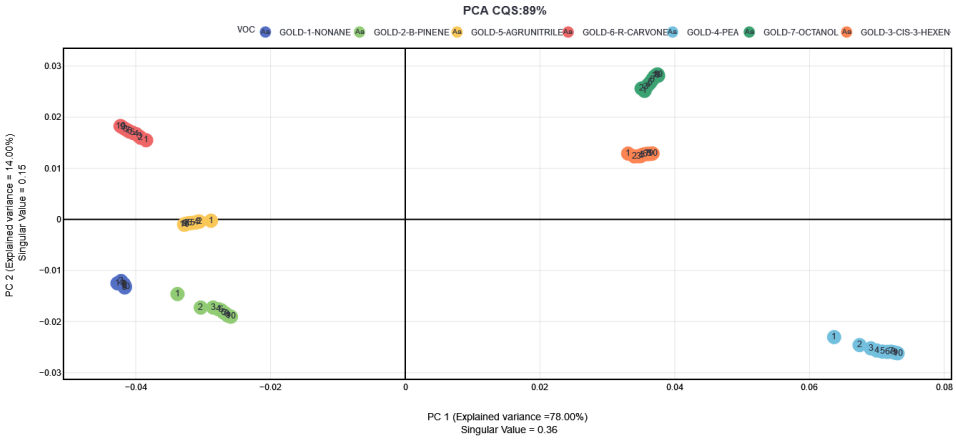

Fig. 11. Principal component analysis of signatures obtained with the measurement of 10 replicates of 7 different VOC.

The performance of an e-nose can be considered as the ability to obtain a unique and repeatable signature for a given odor, as well as the difference of signatures between different odors. This can be easily visualized with a given dataset on a Principal Componant Analysis (PCA) graph. Figure 11 is a PCA of 10 repeated measurements of 7 different VOCs (Nonane, Beta-pinene, agrunitrile, carvone, phenylethanol, octanol, cis-3-hexenol). On this graph, each point is a 64D-signature. The closer the points, the more similar the signatures; the more distant the points, the more different the signatures. The separation between the clusters reflects the good distinction between the signatures of the different tested samples.

The performance of our photonic e-nose mainly relies on three key parameters: 1) Limit of Detection: its ability to detect odors at low concentration; 2) Repeatability: the same odor should

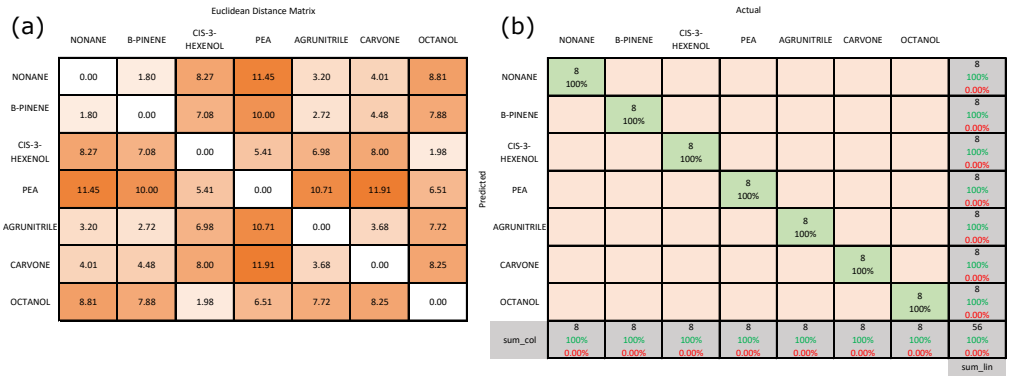

Fig. 12. (a) Distance matrix of signatures obtained with the measurement of 10 replicates of 7 different VOC. (b) Confusion matrix obtained with the same dataset. Training with 2 measurements for each VOC, then tested with the 8 remaining measurements.

lead to the same normalized signature in successive measurements; 3) Contrast: different odors should exhibit different normalized signatures. The contrast can be evaluated by the distance matrix (Figure 12(a)) which represents the average distance between the different classes (here, a class corresponds to a dataset of signatures obtained for a given VOC). Distances can be computed in several ways; here, Euclidian distance is used and is computed as the sum of differences, MZI to MZI, between the normalized signatures of two classes. This matrix is symmetric and the identity of each sample is represented by the diagonal zero value. It is also possible to calculate the average dispersion of each class (called intraclass distance) and to compare this value to the interclass distance. If the interclass distance is superior to the intraclass distance, there is no confusion between the signatures of each class. Practical applications of e-noses depend on their ability to learn and classify odorants. Different learning processes, both supervised and unsupervised, give rise to different machine learning models which are under development and can be embedded into core processes [41]. In this study, with only 20% of the dataset used for the learning phase, it is possible to classify the remaining 80% of measurement with 100% accuracy (Figure 12(b)), which demonstrates the successful operation of our odor sensor.

6. Conclusion

Following our preliminary work on plasmonic-based photonic e-noses [12, 39], this new silicon photonic MZI array-based approach opens up the field of silicon olfactory sensors. The collective manufacturing process results in a remarkable reproducibility and sensibility. The individual biofunctionalization of the MZI sensors generates a contrasted interaction picture when VOC are analyzed. When associated to a training step mimicking the olfactory receptors, these contrasts are the root of the chemical discrimination process. We demonstrated the ability of the sensor to discriminate VOC in ambient condition (humid air) with a ppm range LoD. In the field of quality control of odorant molecules, these fast and reversible binding properties will allow the construction of devices devoted to the high throughput screening of the odorant properties of chemicals. This silicon die is currently the heart of Aryballe's NeOse advanced instrument. The wafer scale production of the present sensors is now fully compatible with low-cost mass production that will open new markets like automotive and consumer devices where performance and cost of the sensors remain a major issue.

Funding

This research has been partially supported by the Nanosciences Foundation (Université Grenoble Alpes), the IRT Nanoelec (ANR-10-AIRT-05) and BPI France (2020-PSPC-5).

Acknowledgments

The authors sincerely acknowledge CEA-Leti silicon fabrication division and Laura Boutafa for their supports with the component fabrication and packaging. The authors thank Liz Facteau for proofreading the article, Jade Gorry for her help with optical characterization and Hayri Okcu for his help with temperature characterization.

Disclosures

CH, JL, DD, BG, TL: Aryballe (F, P).

Data Availability Statement

Data underlying the results presented in this paper are not publicly available at this time but may be obtained from the authors upon reasonable request.

References

1. Eric Mounier and J.-L. Malinge, "From technologies to markets silicon photonics and photonic integrated circuits 2019," Yole Group (2019).
2. J. M. Ramirez, H. Elfaiki, T. Verolet, C. Besancon, A. Gallet, D. Néel, K. Hassan, S. Olivier, C. Jany, S. Malhouitre, K. Gradkowski, P. E. Morrissey, P. O'Brien, C. Caillaud, N. Vaissière, J. Decobert, S. Lei, R. Enright, A. Shen, and M. Achouche, "III-V-on-Silicon Integration: From Hybrid Devices to Heterogeneous Photonic Integrated Circuits," IEEE J. Sel. Top. Quantum Electron. **26** (2020).
3. C. V. Poulton, M. J. Byrd, P. Russo, E. Timurdogan, M. Khandaker, D. Vermeulen, and M. R. Watts, "Long-Range LiDAR and Free-Space Data Communication with High-Performance Optical Phased Arrays," IEEE J. Sel. Top. Quantum Electron. **25** (2019).
4. L. Laplatine, E. Luan, K. Cheung, D. M. Ratner, Y. Dattner, and L. Chrostowski, "System-level integration of active silicon photonic biosensors using Fan-Out Wafer-Level-Packaging for low cost and multiplexed point-of-care diagnostic testing," Sensors Actuators, B: Chem. **273**, 1610–1617 (2018).
5. S. Mudumba, S. de Alba, R. Romero, C. Cherwien, A. Wu, J. Wang, M. A. Gleeson, M. Iqbal, and R. W. Burlingame, "Photonic ring resonance is a versatile platform for performing multiplex immunoassays in real time," J. Immunol. Methods **448**, 34–43 (2017).
6. E. J. Zhang, L. Tombez, J. Orcutt, S. Kamlapurkar, G. Wysocki, and W. M. Green, "Silicon Photonic On-chip Trace-gas Spectroscopy of Methane," in *Conference on Lasers and Electro-Optics,* (OSA, Washington, D.C., 2016), p. SF2H.1.
7. C. Ranacher, A. Tortschanoff, C. Consani, M. Moridi, T. Grille, and B. Jakoby, "Photonic Gas Sensor Using a Silicon Strip Waveguide," Proceedings (2017).
8. J. G. Coutard, M. Brun, M. Fournier, O. Lartigue, F. Fedeli, G. Maisons, J. M. Fedeli, S. Nicoletti, M. Carras, and L. Duraffourg, "Volume Fabrication of Quantum Cascade Lasers on 200 mm-CMOS pilot line," Sci. reports **10**, 6185 (2020).
9. A. D. Wilson and M. Baietto, "Applications and advances in electronic-nose technologies." Sensors (Basel, Switzerland) **9**, 5099–148 (2009).
10. C. Bushdid, M. O. Magnasco, L. B. Vosshall, and A. Keller, "Humans can discriminate more than 1 trillion olfactory stimuli," Science **343**, 1370–1372 (2014).
11. L. Sela and N. Sobel, "Human olfaction: a constant state of change-blindness." Exp. brain research **205**, 13–29 (2010).
12. S. Brenet, A. John-Herpin, F.-X. Gallat, B. Musnier, A. Buhot, C. Herrier, T. Rousselle, T. Livache, and Y. Hou, "Highly-Selective Optoelectronic Nose Based on Surface Plasmon Resonance Imaging for Sensing Volatile Organic Compounds," Anal. Chem. p. acs.analchem.8b02036 (2018).
13. S. Brenet, J. S. Weerakkody, A. Buhot, F.-X. Gallat, R. Mathey, L. Leroy, T. Livache, C. Herrier, and Y. Hou, "Improvement of sensitivity of surface plasmon resonance imaging for the gas-phase detection of volatile organic compounds," Talanta **212**, 120777 (2020).
14. E. Luan, H. Shoman, D. Ratner, K. Cheung, L. Chrostowski, E. Luan, H. Shoman, D. M. Ratner, K. C. Cheung, and L. Chrostowski, "Silicon Photonic Biosensors Using Label-Free Detection," Sensors **18**, 3519 (2018).
15. R. Halir, L. Vivien, X. Le Roux, D. X. Xu, and P. Cheben, "Direct and sensitive phase readout for integrated waveguide sensors," IEEE Photonics J. (2013).

16. J. Leuermann, A. Fernández-Gavela, A. Torres-Cubillo, S. Postigo, A. Sánchez-Postigo, L. M. Lechuga, R. Halir, and Í. Molina-Fernández, "Optimizing the limit of detection of waveguide-based interferometric biosensor devices," Sensors (Switzerland) **19** (2019).
17. R. J. Van Gulik, B. M. De Boer, and P. J. Harmsma, "Refractive Index Sensing Using a Three-Port Interferometer and Comparison with Ring Resonators," IEEE J. on Sel. Top. Quantum Electron. **23** (2017).
18. B. Drapp, J. Piehler, A. Brecht, G. Gauglitz, B. Luff, J. Wilkinson, and J. Ingenhoff, "Integrated optical Mach-Zehnder interferometers as simazine immunoprobes," Sensors Actuators B: Chem. **39**, 277–282 (1997).
19. Í. Molina-Fernández, J. Leuermann, A. Ortega-Moñux, J. G. Wangüemert-Pérez, and R. Halir, "Fundamental limit of detection of photonic biosensors with coherent phase read-out," Opt. Express (2019).
20. N. Fabricius, G. Gauglitz, and J. Ingenhoff, "A gas sensor based on an integrated optical Mach-Zehnder interferometer," Sensors Actuators B: Chem. **7**, 672–676 (1992).
21. N. A. Yebo, W. Bogaerts, Z. Hens, and R. Baets, "On-Chip Arrayed Waveguide Grating Interrogated Silicon-on-Insulator Microring Resonator-Based Gas Sensor," IEEE Photonics Technol. Lett. **23**, 1505–1507 (2011).
22. D. Fu, Q. Liu, J. S. Kee, and M. K. Park, "Silicon microring resonator sensors for the detection of volatile organic compounds," in *2012 Photonics Global Conference, PGC 2012,* (2012).
23. G. Mi, C. Horvath, and V. Van, "Silicon photonic dual-gas sensor for H_2 and CO_2 detection," Opt. Express **25**, 16250 (2017).
24. F. T. Dullo, S. Lindecrantz, J. Jágerská, J. H. Hansen, M. Engqvist, S. A. Solbø, and O. G. Hellesø, "Sensitive on-chip methane detection with a cryptophane-A cladded Mach-Zehnder interferometer," Opt. Express (2015).
25. Y. Chen, W. S. Fegadolli, W. M. Jones, A. Scherer, and M. Li, "Ultrasensitive Gas-Phase Chemical Sensing Based on Functionalized Photonic Crystal Nanobeam Cavities," ACS Nano **8**, 522–527 (2014).
26. G. Antonacci, J. Goyvaerts, H. Zhao, B. Baumgartner, B. Lendl, and R. Baets, "Ultra-sensitive refractive index gas sensor with functionalized silicon nitride photonic circuits," (2020).
27. S. Dante, D. Duval, D. Fariña, A. B. González-Guerrero, and L. M. Lechuga, "Linear readout of integrated interferometric biosensors using a periodic wavelength modulation," Laser Photonics Rev. **9**, 248–255 (2015).
28. P. Xing and J. Viegas, "Broadband CMOS-compatible SOI temperature insensitive Mach-Zehnder interferometer," Opt. Express **23**, 24098 (2015).
29. Y. E. Marin, V. Toccafondo, P. Velha, S. Scarano, S. Tirelli, A. Nottola, Y. Jeong, H. Jeon, S. Kim, M. Minunni, F. Di Pasquale, and C. J. Oton, "Silicon Photonic Biochemical Sensor on Chip Based on Interferometry and Phase-Generated-Carrier Demodulation," IEEE J. Sel. Top. Quantum Electron. **25**, 1–9 (2019).
30. D. Martens, P. Ramirez-Priego, M. S. Murib, A. A. Elamin, A. B. Gonzalez-Guerrero, M. Stehr, F. Jonas, B. Anton, N. Hlawatsch, P. Soetaert, R. Vos, A. Stassen, S. Severi, W. Van Roy, R. Bockstaele, H. Becker, M. Singh, L. Lechuga, and P. Bienstman, "A low-cost integrated biosensing platform based on SiN nanophotonics for biomarker detection in urine," Anal. Methods (2018).
31. P. Muñoz, G. Micó, L. A. Bru, D. Pastor, D. Pérez, J. D. Doménech, J. Fernández, R. Baños, B. Gargallo, R. Alemany, A. M. Sánchez, J. M. Cirera, R. Mas, and C. Domínguez, "Silicon nitride photonic integration platforms for visible, near-infrared and mid-infrared applications," Sensors (Switzerland) (2017).
32. E. Haglund, M. Jahed, J. S. Gustavsson, A. Larsson, J. Goyvaerts, R. Baets, G. Roelkens, M. Rensing, and P. O'brien, "High-power single transverse and polarization mode VCSEL for silicon photonics integration," Opt. Express (2019).
33. P. Muellner, E. Melnik, G. Koppitsch, J. Kraft, F. Schrank, and R. Hainberger, "CMOS-compatible Si3N4 Waveguides for Optical Biosensing," Procedia Eng. **120**, 578–581 (2015).
34. T. Chalyan, L. Pasquardini, F. Falke, M. Zanetti, R. Guider, D. Gandolfi, E. Schreuder, C. Pederzolli, R. G. Heideman, and L. Pavesi, "Biosensors based on Si3N4 asymmetric Mach-Zehnder interferometers," in *Optical Sensing and Detection IV,* vol. 9899 F. Berghmans and A. G. Mignani, eds., International Society for Optics and Photonics (SPIE, 2016), pp. 417 – 425.
35. D. Martens, G. Dong, and P. Bienstman, "Optimized Si3N4 grating couplers for relaxed alignment requirements under flood illumination," Appl. Opt. **56**, 1286 (2017).
36. J. D. Sarmiento-Merenguel, A. Ortega-Moñux, J.-M. Fédéli, J. G. Wangüemert-Pérez, C. Alonso-Ramos, E. Durán-Valdeiglesias, P. Cheben, Í. Molina-Fernández, and R. Halir, "Controlling leakage losses in subwavelength grating silicon metamaterial waveguides," Opt. Lett. **41**, 3443 (2016).
37. M. Scholl, C. Sprossler, M. Denyer, M. Krause, K. Nakajima, A. Maelicke, W. Knoll, and A. Offenhäusser, "Ordered networks of rat hippocampal neurons attached to silicon oxide surfaces," J. neuroscience methods **104**, 65–75 (2000).
38. J. S. Weerakkody, S. Brenet, T. Livache, C. Herrier, Y. Hou, and A. Buhot, "Optical Index Prism Sensitivity of Surface Plasmon Resonance Imaging in Gas Phase: Experiment versus Theory," The J. Phys. Chem. C **124**, 3756–3767 (2020).
39. P. Maho, C. Herrier, T. Livache, P. Comon, and S. Barthelmé, "Real-time gas recognition and gas unmixing in robot applications," Sensors Actuators B: Chem. **330**, 129111 (2021).
40. P. Andrieu, P. É. Billot, J. L. Millot, and T. Gharbi, "Pulse Width Modulation Applied to Olfactory Stimulation for Intensity Tuning," PLOS ONE **10**, e0145373 (2015).
41. P. Maho, C. Herrier, T. Livache, G. Rolland, P. Comon, and S. Barthelmé, "Reliable chiral recognition with an optoelectronic nose," Biosens. Bioelectron. **159**, 112183 (2020).